

Axial Effects in the Taylor-Couette Problem: Spiral-Couette and Spiral-Poiseuille flows

Álvaro Meseguer¹ and Francesc Marquès²

¹ Oxford University Computing Laboratory (Numerical Analysis Group),
Wolfson Building, Parks Road, Oxford OX1 3QD, United Kingdom

² Universitat Politècnica de Catalunya (Departament de Física Aplicada),
Jordi Girona Salgado s/n, Mòdul B4 Campus Nord, 08034 Barcelona, Spain

Abstract. A comprehensive study of the linear stability of the Taylor-Couette problem with imposed axial effects is examined. The study will be focused on two different flows: Spiral Couette (SCF) and Spiral Poiseuille (SPF) flows. In SCF flow, the axial effect is introduced by an inertial axial sliding mechanism between the cylinders. In the SPF, the axial effect is introduced via an imposed axial pressure gradient. For both problems, a wide range of parameters has been explored. In both systems, zeroth order discontinuities are found in the critical stability surface; they are explained as a result of the competition between the centrifugal and shear instability mechanisms, which appears only in the co-rotating case, close to the rigid body rotation region. In both problems, good agreement with the experimental results has been obtained.

1 Introduction

We consider an incompressible viscous fluid which is contained in the gap between two concentric cylinders that rotate independently about a common axis at constant angular velocities. An axial motion is induced by an inertial sliding of the cylinders relative to one another along the pipe axis in the SCF, and by an imposed axial pressure gradient in the SPF case. The basic motions whose linear stability will be studied are, therefore, a superposition of the Couette flow in the azimuthal direction and the axial velocity field induced by the relative sliding, in the former case or by the axial pressure gradient in the second, [13].

The SCF problem was first studied in [15] and [14], where an inviscid stability criteria in the narrow gap case was obtained. The experiments carried out in [14] are, as far as we know, the only experiments made in this problem until now. The general problem was studied in [22] and in [12] with special emphasis in energy methods; an excellent review can be found in [13], chapter VI. In a recent work, [2], a linear stability analysis of the Spiral Couette flow was carried out, in the stationary outer cylinder case, in the so called enclosed geometry, which includes end effects. The more general problem of oscillatory sliding has been recently considered in [11] and [17], whose numerical simulations are in good agreement with the experimental results reported in [28].

The first approaches to the study of the stability of the SPF were carried out in [6] and in [10]. In a more recent study, reported in [25], both numerical and experimental, it was demonstrated that the axial effects may stabilize or

instabilize the basic flow depending on the sign of the speed rotation ratio of the cylinders. Our study provides the first comprehensive numerical exploration of the linear stability of the SPF flow, covering a wide range of angular velocities, being focused on the co-rotation situations because of the presence of new phenomena not observed before. The numerical computations reported here were carried out for the same experimental parameters used in [25].

We have found that SCF and SPF exhibit zeroeth order discontinuities in their critical surface, a result recently reported by the authors in [20] for the SCF. In both cases, this pathology is due to a common fact; the competition between centrifugal and shear instability mechanisms. Mathematically, the spectra of the linear stability operators exhibit radical changes in the space of physical parameters. In other words, the spectra may be, in both problems, split up in two independent subsets, associated to the two instability mechanisms. The behaviour of both subsets is independent of each other, swapping radically their dominance in the transition in different parts of the space of physical parameters.

An understanding of the stability of these flows could have applications in some industrial processes like the purification of industrial waste water, the production of wire and cables and the optical fibre fabrication techniques, see [23], [26] and [4]. In all of them, axial sliding and axial pressure gradients in a cylindrical annulus takes place, and the rotation of one or both cylinders may change the stability and properties of the flow.

The work is structured as follows. Section 2 is devoted to the SCF. In Sec. 2.1 the linear stability in the standard normal mode analysis is formulated. In Sec. 2.2 the difficulties encountered when computing the neutral stability curves, and the algorithms we have used, are described. The linear stability analysis for $\eta = 0.5$ is explained in detail in Sec. 2.3. The mechanism of competition between centrifugal and shear instability mechanisms is explained mathematically as an abnormal behaviour of the topological structure of the neutral stability curves. Comparisons with experimental results for $\eta = 0.8$ are reported in Sec. 2.4. Section 3 is devoted to the linear stability analysis of the SPF. In Sec. 3.1, the stability analysis for $\eta = 0.5$ is reported and comparisons with previous numerical and experimental works are provided.

2 Spiral-Couette Flow

Spiral-Couette flow is the term used to describe fluid motion between two concentric rotating cylinders, whose radius and angular velocities are r_i^* , r_o^* and Ω_i , Ω_o respectively. The annular gap between the cylinders is $d = r_o - r_i$. In addition, the inner cylinder is moving parallel to the common axis with a constant velocity U_c (see Fig. 1). The independent nondimensional parameters appearing in this problem are: the radius ratio $\eta = r_i^*/r_o^*$, which fixes the geometry of the annulus; the Couette flow Reynolds numbers $Ri = dr_i\Omega_i/\nu$ and $Ro = dr_o\Omega_o/\nu$ of the rotating cylinders and the axial Reynolds number $Rz = dU_c/\nu$ measuring the translational velocity of the inner cylinder. Henceforth, all variables will be rendered dimensionless using d , d^2/ν , ν^2/d^2 as units for space, time and the

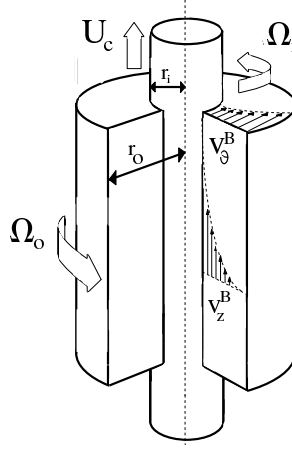


Fig. 1. Physical description of the Spiral-Couette problem. The basic axial-azimuthal flow has also been depicted

reduced pressure (p^*/ϱ^*) . The Navier–Stokes equation and the incompressibility condition for this scaling become

$$\partial_t \mathbf{v} + (\mathbf{v} \cdot \nabla) \mathbf{v} = -\nabla p + \Delta \mathbf{v}, \quad \nabla \cdot \mathbf{v} = 0. \quad (1)$$

Let (u, v, w) the physical components of the velocity \mathbf{v} in cylindrical coordinates (r, θ, z) . The boundary conditions for the flow described above are:

$$u(r_i) = u(r_o) = 0, \quad (2)$$

$$v(r_i) = Ri, \quad v(r_o) = Ro, \quad (3)$$

$$w(r_i, t) = Rz, \quad w(r_o) = 0, \quad (4)$$

where $r_i = \eta/(1 - \eta)$, $r_o = 1/(1 - \eta)$.

In order to compare with experiments and also with previous works, we are going to consider the usually termed *open flow* case. The only experiments of the Taylor–Couette flow with axial sliding of the inner cylinder known to us are those of [14] which were carried out in an annulus with open endwalls. The steady velocity field \mathbf{v}_B , independent on the axial and azimuthal variables, satisfying (1), (2), (3) and (4) is

$$u_B = 0, \quad v_B = Ar + B/r, \quad w_B = C \ln(r/r_o), \quad (5)$$

as can be seen in [13]. The constants A, B, C are given by

$$A = \frac{Ro - \eta Ri}{1 + \eta}, \quad B = \frac{\eta(Ri - \eta Ro)}{(1 - \eta)(1 - \eta^2)}, \quad C = \frac{Rz}{\ln \eta}. \quad (6)$$

2.1 Linear Stability of the SCF.

In the preceding section the basic flow was obtained. We now perturb this basic state by a small disturbance which is assumed to vary periodically in the azimuthal and axial directions:

$$\mathbf{v}(r, \theta, z, t) = \mathbf{v}_B(r) + \mathbf{u}(r)e^{i(n\theta + kz) + \lambda t}, \quad (7)$$

$$p(r, \theta, z, t) = p_B(r, z) + p'(r)e^{i(n\theta + kz) + \lambda t}, \quad (8)$$

where $\mathbf{v}_B = (0, v_B, w_B)$ is given by (5), $n \in \mathbb{N}$, $k \in \mathbb{R}$, $\lambda \in \mathbb{C}$ and the boundary conditions for \mathbf{u} are homogeneous, $\mathbf{u}(r_i) = \mathbf{u}(r_o) = \mathbf{0}$. Linearizing the Navier-Stokes equations about the basic solution, we obtain the eigenvalue problem

$$\lambda \mathbf{u} = -\nabla p' + \Delta \mathbf{u} - \mathbf{v}_B \cdot \nabla \mathbf{u} - \mathbf{u} \cdot \nabla \mathbf{v}_B. \quad (9)$$

In order to solve (9) numerically, a spatial discretization of the problem is accomplished by a solenoidal Petrov-Galerkin scheme [19]. A comprehensive analysis of the method can be found in [21] or [3]. The discretization scheme leads to a generalized eigenvalue problem of the form

$$\lambda G \mathbf{x} = H \mathbf{x}, \quad (10)$$

where matrices G and H explicitly depend on the physical parameters of the problem (see [20], for details).

Let us consider the symmetries of our problem. The Navier-Stokes equations are invariant with respect to the specular reflections $\{z \rightarrow -z, w \rightarrow -w\}$ and $\{\theta \rightarrow -\theta, v \rightarrow -v\}$. They are also invariant with respect to rotations around the axis, axial translations and time translations. The boundary conditions break some of these symmetries. Ri or Ro different from zero breaks the specular reflection $\theta \rightarrow -\theta$, and $Rz \neq 0$ breaks the specular reflection $z \rightarrow -z$. In order to keep the invariance we must change the sign of these Reynolds numbers, and of the corresponding wavenumbers n and k in the solutions of the linearized system (10). Therefore the symmetries allow us to restrict the computations to the cases $Rz > 0$ and $Ri > 0$. Furthermore, since the Navier-Stokes equations are real, the complex conjugate of a perturbation (7, 8) is also a solution, and we can change simultaneously the sign of n , k and the imaginary part of λ . Then we can restrict the computations to the case $k \geq 0$.

When n and k are nonzero, the eigenvector of the linear problem has the form of a spiral pattern (see Fig. 9, showing an experimentally observed spiral flow). The wavenumbers n and k fix the shape of the spiral. The angle α of the spiral with a z -constant plane is given by $\tan \alpha = -n/(r_o k) = -(1 - \eta)n/k$.

If $Rz = 0$, the symmetry $z \rightarrow -z$ is not broken, and at the bifurcation point, in the $n \neq 0$ case, we get two pairs of purely imaginary eigenvalues bifurcating at the same time, representing spirals with opposite slope –or angle– [5]. These spirals have opposite values of n . For $Rz \neq 0$, the corresponding eigenvalues split apart, and one of the two spirals $\pm n$ becomes dominant. Therefore we expect mode competition and switching between $+n$ and $-n$ for Rz close to zero.

2.2 Computation of the Neutral Stability Curves.

It has long been known that whenever two or more control parameters representing different physical mechanisms for instability compete, one can observe stability turning points, islands of stability, multiple minima, and large changes in the critical azimuthal wavenumber. Examples include the competition between buoyancy-induced shear and rotation in radially Couette-flow [1], between rotation and axial sliding in modulated Taylor-Couette flow [17]. In the present problem, the competition between wall-driven shear and centrifugal instability mechanisms will lead to possible hysteresis experimental phenomena.

Let σ be the real part of the first eigenvalue of the linear system (10) which crosses the imaginary axis. The stability of the basic flow is determined by the sign of σ . For negative values of σ , the basic flow is stable under infinitesimal perturbations. When σ is zero or slightly positive, the steady flow becomes unstable and bifurcated secondary flows may appear. It should be remarked that $\sigma(n, k, \eta, Ri, Ro, Rz)$ is a function of the physical parameters which play an essential role in the dynamics of the system. For fixed η, Ro, Rz , and given n, k the inner Reynolds number $Ri_c(n, k)$ such that $\sigma = 0$ is computed. The critical inner Reynolds number is given by $Ri_{crit} = \min_{n,k} Ri_c(n, k)$, and the corresponding values of n, k are the critical azimuthal and axial wavenumbers n_{crit}, k_{crit} which will dictate the geometrical shape of the critical eigenfunction, which may be a spiral flow or travelling Taylor vortices.

The curves in the (k, Ri) plane given by $\sigma(k, Ri) = 0$ are commonly termed Neutral Stability Curves (NSC). The main goal at this stage is to compute the absolute minimum of the NSC, which will give the critical parameters (k_{crit}, Ri_{crit}) – in fact, the absolute minimum of the set of the NSC corresponding to integer values of n will be found. As it will be seen later, the NSC curves for this problem may have multiple extrema (maxima and minima), exhibit disconnected parts and sharp geometrical forms. Furthermore, these curves may exhibit multivalued branches as functions of k , and these features can change abruptly in some parameter ranges (see Fig. 2). Standard methods applied to a regular grid in the plane (k, Ri) require exorbitantly high accuracy computations. Consequently, an alternative 2-dimensional Newton-Raphson method has been used; see [19] for details.

2.3 Stability analysis for $\eta = 0.5$

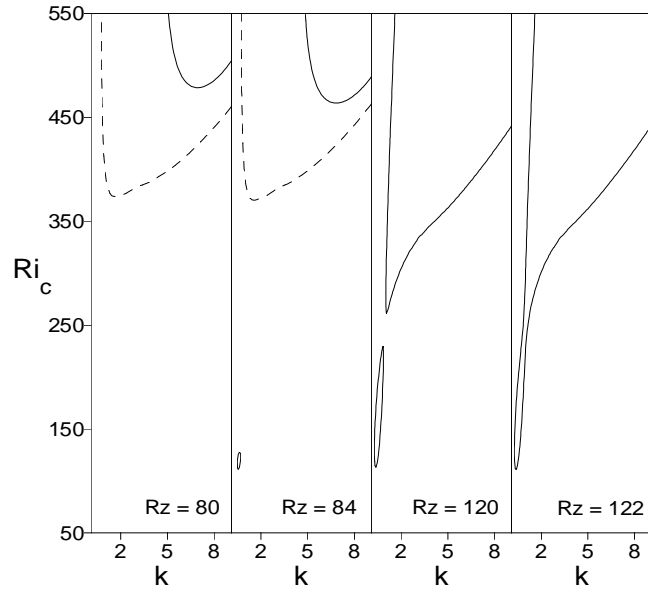
The computation of $Ri_c(Rz, Ro)$ for the wide gap $\eta = 0.5$, gives as a first striking result the presence of a zeroth-order discontinuity in Ri_c , in the co-rotating case ($Ro > 0$). Although this behavior has been considered possible by some authors, [7], specific examples showing this kind of discontinuity are very unusual in the fluid mechanics literature.

For $Ro = 200$ the discontinuity appears for $Rz = 82.63$. We have shown in Fig. 2a the critical Ri as a function of k . For $Rz = 80$ the dominant mode is $n = -1$, giving $Ri_c = 373.43$ and $k_c = 1.68$; but for $Rz = 82.63$ the marginal stability curve of the $n = -4$ mode develops an island of instability for a much

lower $Ri_c = 119.13$, introducing a discontinuity in Ri_c . Notice too that the change in n_{crit} is not ± 1 as usual, but it changes in three units. The island of instability is very small (Fig. 2a, $Rz = 84$), becoming larger when we move away of the discontinuity. All these features make the numerical computation of the critical parameters very difficult from the algorithmic point of view. For these reasons we have developed specific numerical methods, outlined in [20], in order to detect the islands as soon as they appear. Similar islands of instability have been found in [17]. Before crossing the Ri_c discontinuity, the marginal stability curve for $n = -4$ has a single extrema, a minimum (Fig. 2a, $Rz = 80$), giving the critical parameter values (Ri_c, k_c) . After crossing, and due to the appearance of the island, we have three extrema, two minima and a maximum, and the marginal stability curve has two disconnected branches. If we move to higher Rz values, the island grows until it merges with the other branch (Fig. 2a, $Rz = 120, 122$); the marginal curve has now a single minimum. Plotting the position of all the extrema as a function of Rz , we get an S-shaped curve, displayed in Fig. 2b; the solid curve gives the absolute minimum, and the dashed curve corresponds to the other extrema. The critical Reynolds number Ri_c becomes discontinuous (zeroth order discontinuity) as soon as the island of instability appears for $Rz = 82.64$; experiments made by increasing Ri and Rz held fixed would report the solid curve in Fig. 2b. The whole critical surface is multivalued and continuous, but is folded in such a way that a cusp develops; Fig. 3a shows a perspective view of the critical surface. Fig. 3b shows the same critical surface with the curves corresponding to a change in the critical azimuthal wavenumber n , where the surface is not smooth (the tangent plane is discontinuous along these curves). The projection of the curves corresponding to a change in the azimuthal wavenumber n are plotted in Fig. 4. The edges of the cusp region are plotted as thick lines in both Figs. 3b and 4. These discontinuities and fold structure may have important consequences which could be detected experimentally, like hysteresis phenomena, as well as the discontinuity in Ri_c .

Fig. 2.3 shows Ri_c and α as a function of Ro for different values of Rz . The critical Reynolds number Ri_c (Fig. 2.3a) is almost independent of Rz in the counter-rotating region $Ro < 0$. But in the co-rotating region, where the cusp develops, we have two well-separated kinds of behavior. This figure is a front view of the cusp structure (Fig. 3) along the Rz axis. For small axial sliding Rz , before the discontinuity, Ri_c is very close to the values without sliding (Taylor-Couette flow). For higher axial sliding, after the discontinuity, Ri_c falls to much lower values. The axial sliding is destabilizing, except in the small region where the axisymmetric mode ($n = 0$) is dominant. The destabilizing effect becomes significant only in the co-rotating case, after the discontinuity. The centrifugal instability seems to be the dominant mechanism (as in Taylor-Couette, $Rz = 0$) except after the discontinuity, where a shear instability due to the axial sliding becomes dominant; the cuspidal zone can be thought as the transition region between both mechanisms. This qualitative change can also be noticed in the angle of the spiral pattern α (Fig. 2.3c), which jumps from values less than 0.2 radians (10°) to values close to 1.2 radians (70°). We also notice that the shear-

(a)



(b)

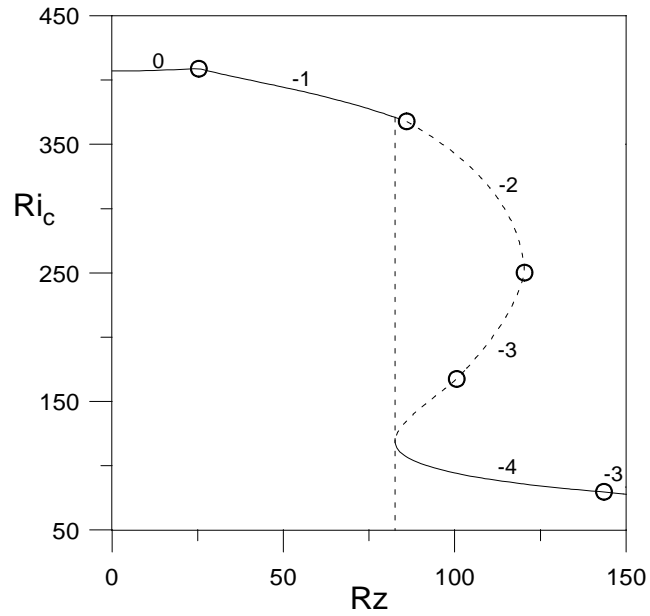
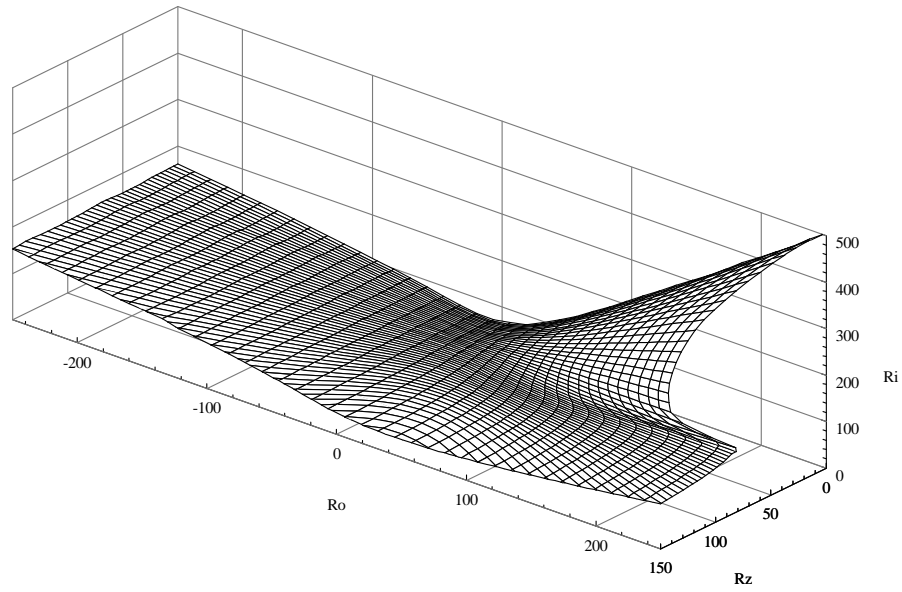


Fig. 2. (a) Formation and evolution of an island of instability for $\eta = 0.5$ and the dashed one to $n = -1$. (b) The corresponding critical inner Reynolds number Ri_c as a function of Rz (solid line); the dashed line is a section ($Ro = 200$) of the critical surface (Fig. 5). The labels refer to the dominant azimuthal mode number n ; the hollow circles are the transitions between different n . Ri_c is discontinuous for $Rz = 82.64$

(a)



(b)

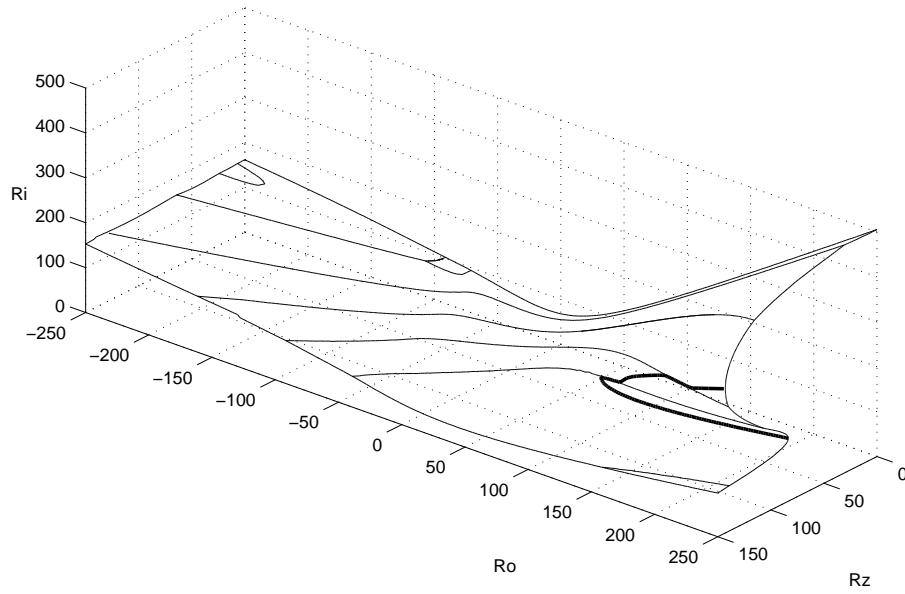


Fig. 3. (a) Perspective view of the critical surface $Ri_c(Ro, Rz)$ for $\eta = 0.5$ (b) Same view, explicitly showing the changes in the dominant azimuthal mode n at criticality. The edges of the cusp region are also plotted as thick lines

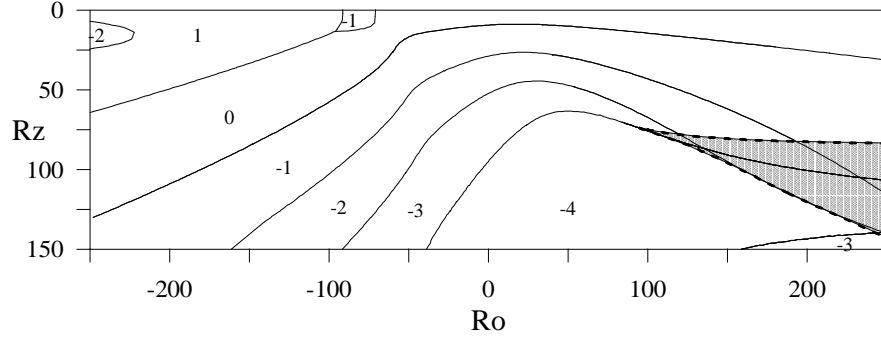


Fig. 4. Dominant azimuthal mode n at criticality, as a function of Ro , Rz ; $\eta = 0.5$. The shaded region corresponds to the fold, whose edges are plotted as thick dashed lines

instability dominated branch is very close to the solid body rotation line (see Fig. 2.3a), where the centrifugal instability does not play a significant role; see [16]. Figure 6 shows Ri_c and α as a function of Rz for different values of Ro

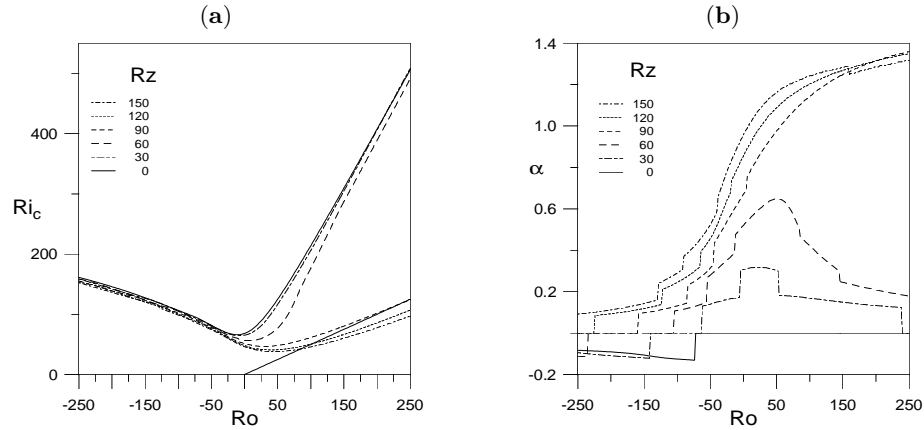


Fig. 5. Critical parameters for $\eta = 0.5$, as functions of the outer Reynolds number Ro . (a) Critical inner Reynolds number Ri_c ; the solid straight line is the rigid rotation line $Ri = \eta Ro$. (b) Angle of the spiral pattern α in radians

in the co-rotating case. In Fig. 6a sections of the cusp region are displayed; the critical Ri_c is in fact the minimum of the values in the multivalued region, so we have a discontinuity which grows when increasing Ro . The discontinuity has been displayed in Fig. 6b.

The bicritical points where the azimuthal wavenumber n changes and two eigenvalues bifurcates simultaneously are distinguished with a vertical bar. The effect of the sliding on these axisymmetric modes is slightly stabilizing, in con-

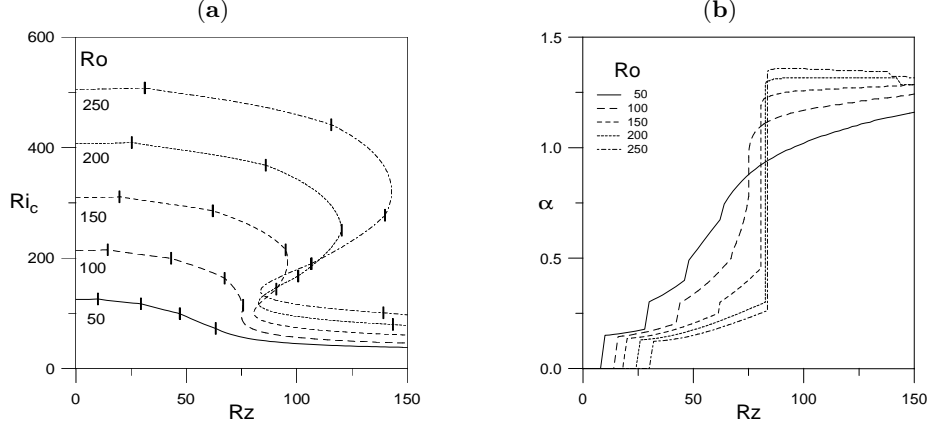


Fig. 6. Critical parameters for $\eta = 0.5$, as functions of the axial Reynolds number Rz in the co-rotating case $Ro > 0$. (a) Critical inner Reynolds number Ri_c . (b) Angle of the spiral pattern α in radians

trast to their destabilizing effect on the non-axisymmetric modes, mainly in the co-rotating region, an effect also reported by [2].

2.4 Comparison with experimental results ($\eta = 0.8$)

Some previous experimental studies have been reported on the stability of the spiral Couette flow. In fact, in an excellent study done in [14], both theoretical and experimental, a stability analysis has been devoted to an specific zone on the parameter space, inside the cusp region. The experimental apparatus has a gap $\eta = 0.8$, with open ends, corresponding to our open flow case. The rotational speed of the external cylinder is held fixed at $Ro \approx 750$. Ludwig's experimental device needed high external rotation speeds in order to avoid pre-turbulent stages induced by transients. The unique design of the experimental apparatus enforced a linear dependence between axial velocity and azimuthal rotation speed of the inner cylinder moving relative to an outer stationary cylinder (without axial velocity but rotating). As a result, the experimental paths in the parameter space (Ri, Rz) were straight lines, as can be seen both in figs. 7, 8. Ludwig's experimental results (Fig. 7) are given in terms of two nondimensional parameters \tilde{c}_ϕ and \tilde{c}_z which describe the motion of the fluid. As in [12], we have used the values of \tilde{c}_ϕ , \tilde{c}_z to compare with Ludwig's results. A more detailed discussion about the parameters used by different authors is given in [20]. The dependence between \tilde{c}_ϕ , \tilde{c}_z and our variables Ri , Ro , Rz are given by the following equations (for $\eta = 0.8$):

$$\tilde{c}_\phi = \frac{1 + \eta}{1 - \eta} \frac{Ro - Ri}{Ro + Ri}, \quad \tilde{c}_z = \frac{1 + \eta}{1 - \eta} \frac{Rz}{Ro + Ri}. \quad (11)$$

For the $\eta = 0.8$ case the narrow gap approximation is not clearly justified. This can be a source of error in the experimental values given by [14]. It would be

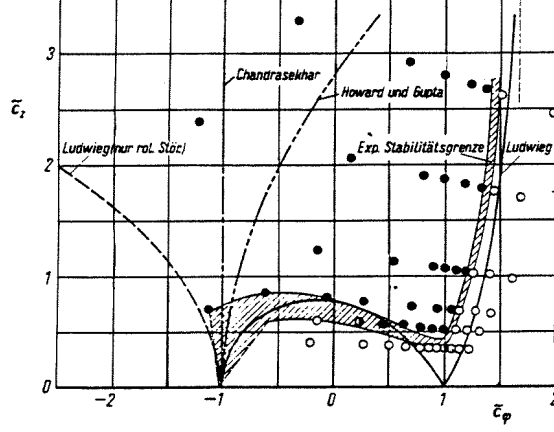


Fig. 7. Ludwig experiments. Experimental results, from [14]; $\eta = 0.8$, $Ro = 750$

necessary to know the original experimental results in terms of the Reynolds numbers in order to work with the *true* control parameters Rz and Ri .

The experimental results of Ludwig are summarized in Fig. 7. The shaded area is the error bandwidth experimentally obtained. These errors are very large in the fold region of the critical surface, and the reasons will be analyzed shortly thereafter. Figure 7 also shows several stability criteria. Three of them, labelled *Ludwig (nur rot. Stöc)*, *Chandrasekhar* and *Howard und Gupta*, were obtained assuming axisymmetric perturbations, and using physical considerations as in the Rayleigh's criterion (labelled *Chandrasekhar* in Fig. 7). All of them are in very poor agreement with the experimental data. Instead, Ludwig's stability criterion, obtained by exactly solving the linearized Euler equations in the narrow gap limit, is reasonably close to the experimental data.

A linear stability analysis of the Spiral Couette problem was reported by Hung, Joseph & Munson (1972) (referred from now on as HJM), where only particular regions in parameter space were considered. Their results are in good agreement with some of Ludwig's results, although there were some unexplored zones that the present work has studied in detail. We have computed the critical curve for $Ro = 750$, which is single-valued considering $Rz(Ri)$, but it is well within the cusp region. The joint results of the three analyses have been sketched in Fig. 8, which corresponds to the section $Ro = 750$ of the critical surface. Our results are fully coincident with the previous computations of HJM, except for two points on the left of the minimum of our critical curve in Fig. 8, where the results of HJM clearly diverge from the experimental results. It is apparent that the results of HJM are confined to the intermediate branch of the critical surface fold, where the changes in Rz_c are small. The other branches shows

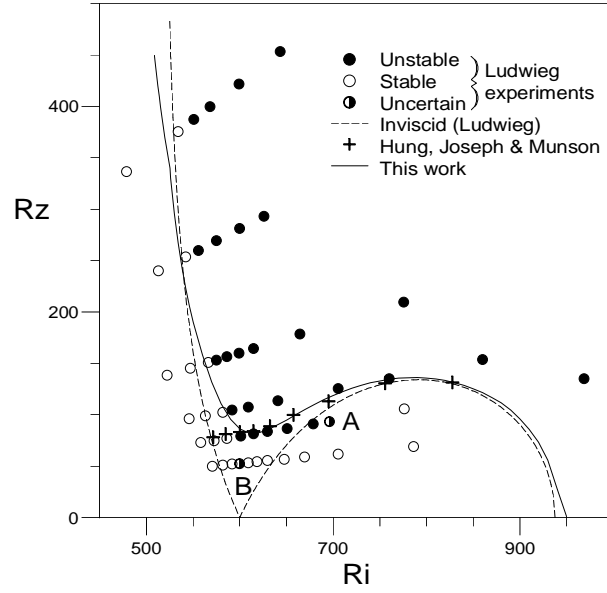


Fig. 8. Comparison between the experimental and theoretical results of Ludwig (1964), Hung, Joseph & Munson (1972) and the present work. Parameters: $\eta = 0.8$, $Ro = 750$

very high slopes of $Rz_c(Ri)$; furthermore, the change in the critical azimuthal wavenumber n is of more than 15 units in this range. This is an indication of the difficulties HJM encountered outside the intermediate branch, which explains the discrepancy of their two computed points in the high slope region of the stability curve. The experimental results of Ludwig show remarkable agreement with our

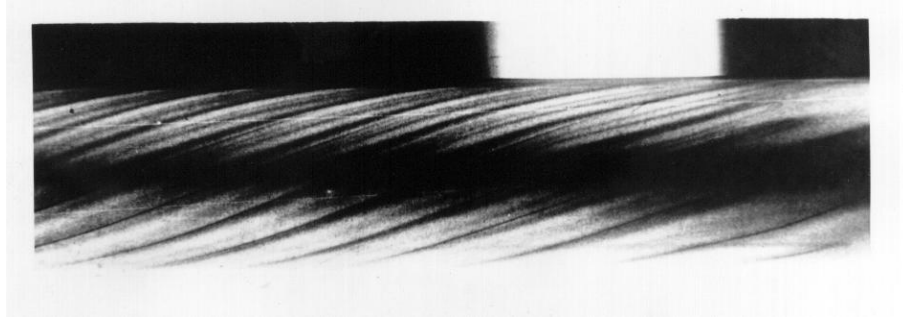


Fig. 9. Ludwig experiments. Picture of the spirals, from [27]

numerical results. The best experimentally defined bifurcation points correspond

to the vertical branch (where shear is the dominant instability mechanism), and on this curve the discrepancies with our results are less than 4%; we must mention that this is the first time the vertical branch has been computed numerically. In the region close to the minimum of the critical curve, the onset of instability is in very good agreement with the experiments, but some points on the right side of the minimum clearly deviate from the numerical predictions. Notice that the points A and B, marked with a black and white circle, where Ludwig could not decide about their stability, are very close to the hysteresis region, strongly suggesting that the bifurcation could be subcritical in this region of parameter space. Ludwig acknowledged the experimental uncertainties in this parameter region; Fig. 7b shows the estimated uncertainty as a dashed area. For a detailed explanation of Ludwig's experimental procedure, see [14] or [20].

3 Spiral-Poiseuille Flow

The first study of the stability of the spiral Poiseuille problem against three-dimensional perturbations, was carried out in [6] and in [10]. In [6], a monotonical dependence between the critical parameters was assumed for axisymmetric and non-axisymmetric perturbations. In a more recent study, reported by Takeuchi & Jankowski in 1981, [25], both numerical and experimental, it was demonstrated that the axial effects may stabilize or instabilize the basic flow depending on the sign of the speed rotation ratio of the cylinders. Takeuchi & Jankowski (TJ) experiments, are, as far as we know, the most recent ones and they were carried out for the wide gap $\eta = 0.5$ case and for three different azimuthal angular speed ratios of the cylinders ($\mu = \Omega_o/\Omega_i = 0, 0.2, -0.5$).

A comprehensive numerical exploration of the linear stability of the spiral Poiseuille flow is presented, covering a wide range of angular velocities, and being focused on the co-rotation situations because of the presence of new phenomena not observed before experimentally. The numerical computations were carried out for the same wide gap case ($\eta = 0.5$) studied in [25] in order to compare our numerical results with the experimental ones.

The independent nondimensional parameters appearing in this problem are the same described SCF, where the axial sliding effect R_z is no longer present, but replaced by the *Poiseuille* number, $P = (\partial_z P^*)(r_o - r_i)^3/\rho\nu^2$, measuring the imposed axial pressure gradient. A physical description of the problem can be found in Fig. 10. As in the SCF, the azimuthal component of the basic vector field is dictated by the Couette flow. The axial basic flow, represented in Fig. 10, is now a superposition of logarithmic and parabolic profiles. The explicit expressions for the basic flow can be obtained under the same symmetry assumptions that in SCF; see [13]:

$$u_B = 0, \quad v_B = Ar + \frac{B}{r}, \quad w_B = C \ln\left(\frac{r}{r_o}\right) + \frac{P}{4}(r^2 - r_o^2), \quad (12)$$

where the constants A , B and C are

$$A = \frac{Ro - \eta Ri}{1 + \eta}, \quad B = \frac{\eta(Ri - \eta Ro)}{(1 - \eta)(1 - \eta^2)}, \quad C = \frac{1}{\ln \eta} \frac{P(1 + \eta)}{4(1 - \eta)}. \quad (13)$$

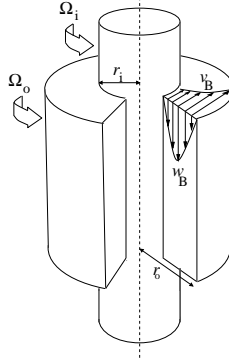


Fig. 10. Physical description of the Spiral-Poiseuille problem. The basic axial-azimuthal flow has also been depicted

3.1 Linear stability results ($\eta = 0.5$)

As before, the basic spiral Poiseuille flow $\mathbf{v}_B = (0, v_B, w_B)$ is perturbed by a small disturbance which is assumed to be periodic in the azimuthal and axial variables. The linear stability analysis is carried out by the same solenoidal Petrov-Galerkin scheme, [19], already used in the analysis of the sliding case, SCF, Sec. 2. The linear stability of the SPF has been explored in the range of values $Ro \in [0, 450]$, $P \in [0, 1500]$ and $Ri \in [0, 900]$. The numerical algorithm used to compute the neutral stability curves and their minima is the same that was used in [20]. For each pair of values (P, Ro) , the critical inner Reynolds number Ri_c and the critical axial wavenumber k_c are computed for different values of the azimuthal wave-number n . The selection of the minimum Ri value leads to a functional dependence $Ri_c = f(P, Ro)$. Geometrically, the function f defines a surface in the parameter space which is usually termed *marginal* or *critical* surface. This surface is not regular, being not differentiable in the points where the change of azimuthal dominance take place. This is a common feature in hydrodynamic stability. In Fig. 11, Ro -constant sections of the critical surface have been depicted for low outer rotations. It can be observed that the axial pressure gradient has a stabilization effect over the axisymmetric and non-axisymmetric perturbations with low azimuthal wave number ($|n| \leq 3$). Nevertheless, for higher values of Ro , the transition curves exhibit multiplicity with respect to the variable P and zeroth-discontinuities due to the competition between centrifugal and shear instability mechanisms. Mathematically, this phenomenon has the same explanation as in the SCF.

Figures 12a-d show the formation of an island of instability as long as the Poiseuille number is increased, for a fixed outer rotation Reynolds number ($Ro = 450$). Initially, for $P = 1000$, the dominant azimuthal mode is $n = -3$, see Fig. 12a. For $P = 1100$, an island of instability appears. This island is associated to another azimuthal mode ($n = -6$), being dominant and lowering radically the critical Ri value in a factor of four approximately, see Fig. 12b. As long as

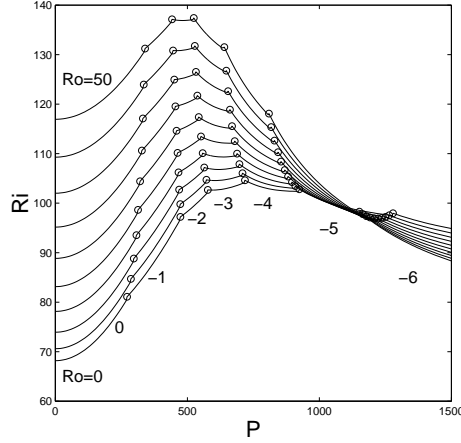


Fig. 11. Ro -constant sections of the critical surface for low outer rotations. The curves correspond to the values $Ro = 5, 10, \dots, 50$. The circles have been plotted in the transitions of azimuthal dominance $n = 0, -1, -2, \dots$. The first curve $Ro = 0$ agrees with [25] (case $\mu = 0$)

P is increased, the island grows in size, and eventually merges with the upper branch of the $n = -6$ mode, as shown in Fig. 12c and Fig. 12d. Altogether, this mechanism leads to the presence of a folding in the critical surface, in the same way as it appeared in the SCF. As it can be observed in Fig. 13, the critical curves exhibit a folding as long as the outer rotation Ro parameter is increased. Figure 13 is a cross section of the critical surface plotted in Fig. 14 for different values of Ro . For $Ro > 250$, the critical curves exhibit a multivalued branch which can not be computed as a function of P . Therefore, Ri is the fixed parameter in those branches, being $P_{crit.}$ the sought value for instability. The whole phenomena can be observed globally in Fig. 14. This anomalous behaviour has been already reported numerically in [20] and experimentally in [14] for the spiral Couette flow.. Apparently, this anomaly was not detected in TJ experiments because they worked in restricted planes $Ro = \mu\eta Ri$. In Fig. 14, we have indicated two curves, named TJ1 and TJ2, which correspond to the numerical and experimental exploration made by Takeuchi & Jankowski for their cases $\mu = 0$ and $\mu = 0.2$, respectively. As depicted in Fig. 14, TJ numerical and experimental exploration range is far away from the cuspidal zone where the folding appears. The projection of the transition curves between different azimuthal wavenumbers n has been plotted in Fig. 15. The projection of the curves of maxima (M) and minima (m) of Fig. 14, which are the boundary of the cuspidal zone, and where hysteresis phenomena may appear, are also included in Fig. 15. Similar computations, not reported here, were done in the *counter-rotation* ($Ri Ro < 0$) situations. Due to the dominance of the centrifugal instability mechanism in this region, the critical surface exhibits a quite regular behaviour, as in the SCF.

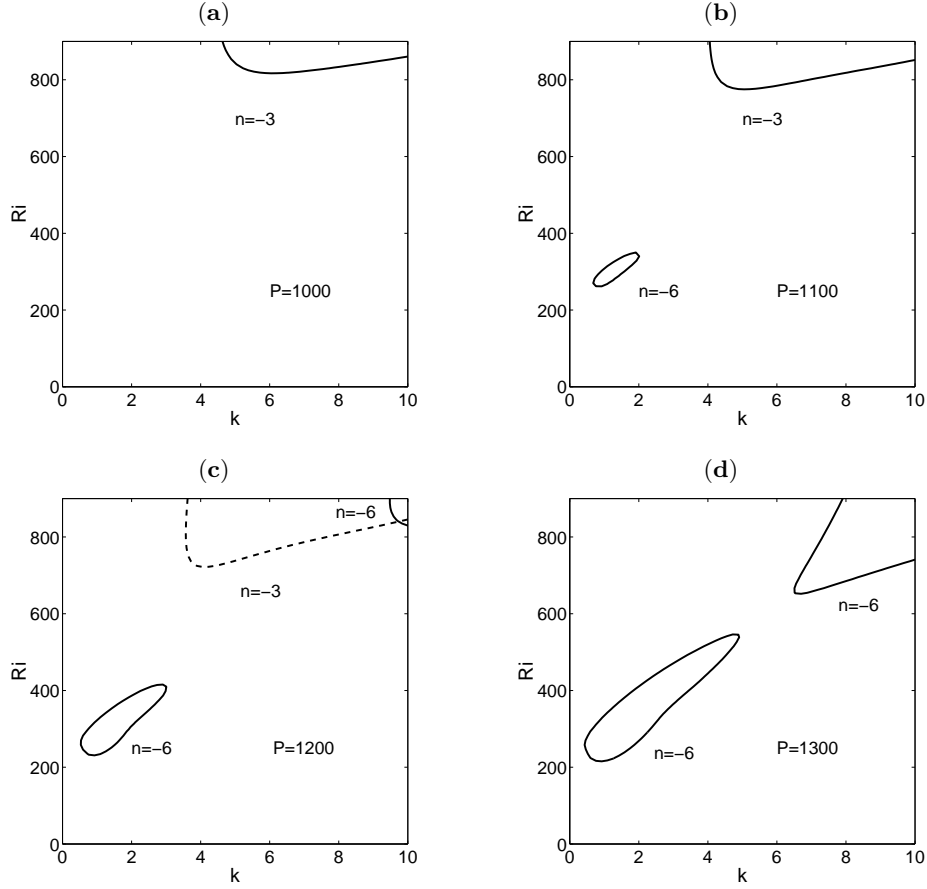


Fig. 12. Formation of an island of instability in the SPF for $Ro = 450$

4 Conclusions.

A comprehensive exploration of the linear stability of the Taylor-Couette flow with imposed axial effects has been done. The study has been focused in two particular problems, the Spiral Couette and Spiral Poiseuille flows. In both problems, complex critical behaviour has been detected for co-rotation situations. The critical surfaces $Ri_c = f(Rz, Ro)$ and $Ri_c = f(P, Ro)$ exhibit zeroeth order discontinuities which can only be detected making use of a specifically tailored, efficient and robust numerical scheme for the computation of the neutral stability curves. This unusual phenomena in hydrodynamical stability problems has been explained in terms of competition between two independent instability mechanisms: in the current problems the centrifugal instability, dominant in the counter-rotating regime and also for small axial effect, competes with the shear instability induced by the axial motion. For the Spiral Couette flow, experimental evidences confirm this anomalous behaviour. For this problem, our numerical

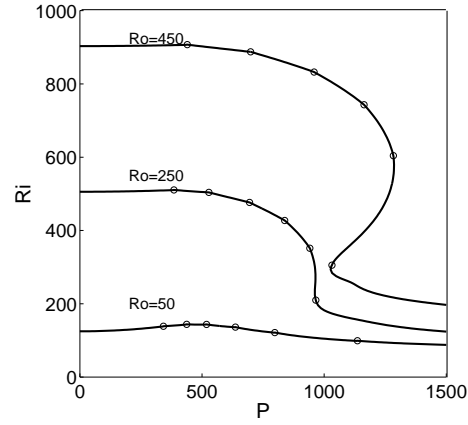


Fig. 13. Formation of the folding in the Spiral-Poiseuille Flow for higher outer rotation Reynolds numbers Ro

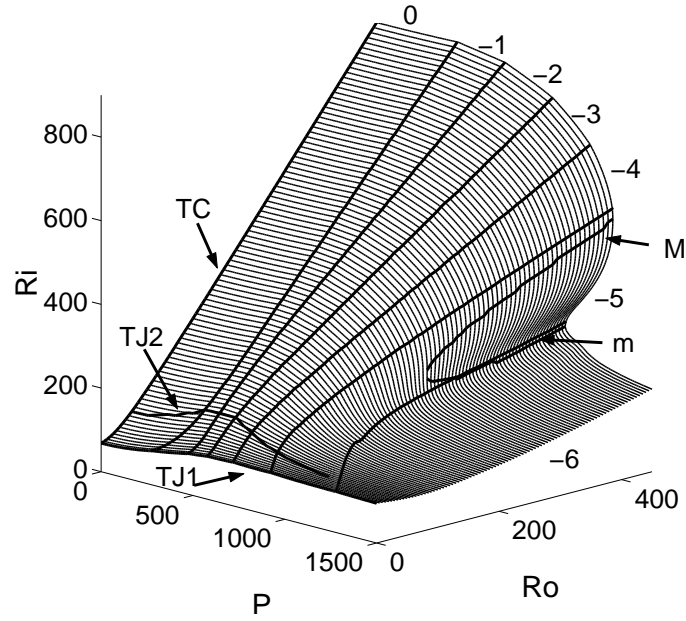


Fig. 14. Critical surface for the co-rotating Spiral-Poiseuille Flow. The label TC stands for the Taylor-Couette curve ($P = 0$) which asymptotically tends to the Rayleigh's inviscid criterion of instability. TJ1 and TJ2 stand for numerical and experimental explorations carried out in [25] for $\mu = 0$ and $\mu = 0.2$, respectively. M and m stand for the curves of maxima and minima over the folding which form the boundary of the cuspidal region

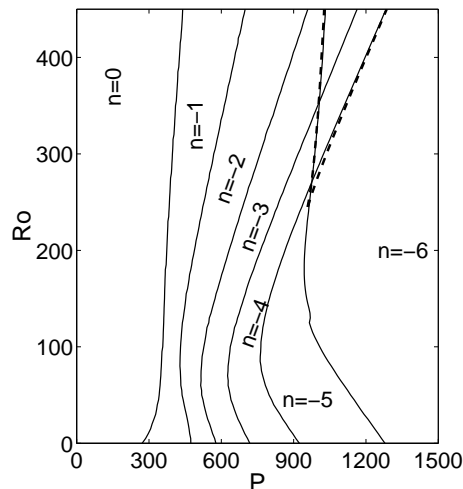


Fig. 15. Projection of the transition curves between different dominant azimuthal modes n . The dashed lines correspond to the projection of the curves M and m from Fig. 14

computations are in complete agreement with the experimental results and with previous numerical approaches. For the Spiral Poiseuille flow, additional experiments would be required to confirm the presented computations. Overall, both problems would require suitable experimental procedures (i.e. independence between axial and azimuthal speeds) in order to properly detect the first instability of the basic spiral flow, and explore the competition between the different instability mechanisms in the fold region.

References

1. M.E. Ali, P.D. Weidman: *J. Fluid Mech.*, **220** 53-84 (1990)
2. M.E. Ali, P.D. Weidman: *Phys. Fluids A* **5** 1188-1200 (1993)
3. C. Canuto, M.Y. Hussaini, A. Quarteroni, T.A. Zang: *Spectral Methods in Fluid Dynamics*. (Springer Series in Computational Physics, 1988) ‘
4. K. Chida, S. Sakaguchi, M. Wagatsuma, T. Kimura: *Electronic Letters*, **18**, 713-715 (1982)
5. P. Chossat, G. Iooss: *The Couette-Taylor Problem*. Applied Mathematical Sciences, **102**, Springer-Verlag, New York (1994)
6. K. C. Chung & K. N. Astill: *J. Fluid Mech.* **81** 641-655 (1977)
7. S.H. Davis & S. Rosenblat: *Studies App. Math.*, **57**, 59-76 (1977)
8. W.S. Edwards, R.P. Tagg, B.C. Dornblaser, H.L. Swinney: *Eur. J. Mech. B Fluids*, **10**, 205-210 (1991)
9. J.E. Hart: *J. Fluid Mech.*, **47**, 547-576 (1971)
10. M. A. Hasoon and B. W. Martin: *Proc. R. Soc. Lond. A*, **352**, 351-380 (1977)
11. H.C. Hu, R.E. Kelly: *Phys. Rev. E*, **51**, 3242-3251 (1995)

12. W.L. Hung, D.D. Joseph, B.R. Munson: J. Fluid Mech., **51**, 593–612 (1972)
13. D. D. Joseph: *Stability of Fluid Motions* vol. I and II (Springer-Verlag, Berlin 1976)
14. H. Ludwig: Z. Flugwiss., **12**, 304–309 (1964)
15. I. Kiessling: Duetsche Versuchsanstalt fur Luft-Unraumfahrt—Bericht 290 (1963)
16. P.A. Mackrodt: J. Fluid Mech., **73**, 153–164 (1976)
17. F. Marques and J.M. Lopez: J. Fluid Mech., **348**, 153–175 (1997)
18. G.B. McFadden, S.R. Coriell, B.T. Murray, M.E. Glicksman and M.E. Selleck: Phys. Fluids **A2**, 700–705 (1990)
19. A. Meseguer: Bifurcations in Fluid Systems: Petrov-Galerkin Schemes. Thesis, Universitat Politècnica de Catalunya, Barcelona (1998)
20. A. Meseguer, F. Marques: J. Fluid Mech., **402**, 33–56 (2000)
21. R.D. Moser, P. Moin, A. Leonard: J. Comput. Phys. **52**, 524–544 (1983)
22. J.E. Mott, D.D. Joseph: Phys. Fluids **11**, 2065–2073 (1968)
23. D.F. Ollis, E. Pelizzetti, N. Serpone: Environ. Sci. Technol., **25**, 1523–1529 (1991)
24. J. Sanchez, D. Crespo & F. Marques: App. Sci. Res., **51**, 55–59 (1993)
25. D. I. Takeuchi & D. F. Jankowski: J. Fluid Mech. **102**, 101–126 (1981)
26. Z. Tadmor, R.B. Bird: Polymer Eng. and Sci., **14**, 124–136 (1974)
27. E. Wedemeyer: AVA—Bericht 67, A34 (1967)
28. A.Y. Weisberg, A. Smits & I. Kevrekidis: J. Fluid Mech., **348**, 141–151 (1997)